

---

This is an electronic reprint of the original article.  
This reprint may differ from the original in pagination and typographic detail.

Zhong, Shuomin; Wang, Xuchen; Tretyakov, Sergei A.

## Coherent Control of Wave Beams Via Unidirectional Evanescent Modes Excitation

*Published in:*  
Advanced Functional Materials

*DOI:*  
[10.1002/adfm.202304300](https://doi.org/10.1002/adfm.202304300)

Published: 23/11/2023

*Document Version*  
Peer-reviewed accepted author manuscript, also known as Final accepted manuscript or Post-print

*Please cite the original version:*  
Zhong, S., Wang, X., & Tretyakov, S. A. (2023). Coherent Control of Wave Beams Via Unidirectional Evanescent Modes Excitation. *Advanced Functional Materials*, 33(48), Article 2304300.  
<https://doi.org/10.1002/adfm.202304300>

---

This material is protected by copyright and other intellectual property rights, and duplication or sale of all or part of any of the repository collections is not permitted, except that material may be duplicated by you for your research use or educational purposes in electronic or print form. You must obtain permission for any other use. Electronic or print copies may not be offered, whether for sale or otherwise to anyone who is not an authorised user.

# Coherent control of wave beams via unidirectional evanescent modes excitation

Shuomin Zhong,<sup>\*,†</sup> Xuchen Wang,<sup>\*,‡</sup> and Sergei A. Tretyakov<sup>¶</sup>

<sup>†</sup> *School of Information Science and Engineering, Ningbo University, Ningbo 315211, China; <https://orcid.org/0000-0001-9860-1741>*

<sup>‡</sup> *Institute of Nanotechnology, Karlsruhe Institute of Technology, 76131 Karlsruhe, Germany*

<sup>¶</sup> *Department of Electronics and Nanoengineering, Aalto University, Finland*

E-mail: zhongshuomin@nbu.edu.cn; xuchen.wang@kit.edu

## Abstract

Conventional coherent absorption occurs only when two incident beams exhibit mirror symmetry with respect to the absorbing surface, i.e., the two beams have the same incident angles, phases, and amplitudes. In this work, we propose a more general metasurface paradigm for coherent perfect absorption, with impinging waves from arbitrary asymmetric directions. By exploiting excitation of unidirectional evanescent waves, the output can be fixed at one reflection direction for any amplitude and phase of the control wave. We show theoretically and confirm experimentally that the relative amplitude of the reflected wave can be tuned continuously from zero to unity by changing the phase difference between the two beams, i.e. switching from coherent perfect absorption to full reflection. We hope that this work will open up promising possibilities for wave manipulation via evanescent waves engineering with applications in optical switches, optical computing, one-side sensing, photovoltaics and radar cross section control.

# Introduction

Coherent control of propagation of a wave beam by tuning the amplitude and phase of another beam is a very promising approach to realize ultra fast optical devices for optical computing, sensing, and other applications.<sup>1-11</sup> One of the most important effects in coherent control of light is coherent perfect absorption.<sup>12-19</sup> In these devices, the level of absorption of one beam illuminating a thin sheet is controlled by another coherent beam that illuminates the same sheet. In earlier works, coherent perfect absorption (CPA) was achieved only when with illumination from different sides of a homogeneous lossy layer and for two incident waves at the same angle.<sup>12,13,15,19</sup> The mechanism of coherent perfect absorption is destructive cancellation of all scattered beams. For homogeneous coherent perfect absorbers, there are only specular reflection and non-diffractive transmission, allowing coherent absorption only with illumination of both sides and at the same incidence angle. From the theoretical point of view and for many applications, it is important to achieve coherent control of output for illuminations from the same side of the metasurface sheet at two or more arbitrary incidence angles.

In this decade, the emergence of gradient metasurfaces<sup>20-27</sup> and metagratings<sup>28-37</sup> has opened a new avenue for manipulation of light for arbitrary incidence angles and versatile functionalities. For periodical metasurfaces or metagratings with the period larger than half of the wavelength, the incident plane wave from one direction will be scattered into multiple directions, and the power carried by the incident wave can be redistributed among a number of diffraction modes. Based on this concept, several metasurface devices with perfect anomalous reflection working at microwaves<sup>38,39</sup> and optical bands<sup>40</sup> have been developed. However, in these previous works, the functionality of metasurfaces is designed only for one incident angle and the response for other illuminations is actually not considered. To design metasurfaces with coherent control functions for multiple simultaneously incident coherent beams from different directions, the matching conditions of amplitude, phase, and wavevector(direction) of the scattering modes between all incidences are required,<sup>36,41,42</sup>

which is almost an impossible task using traditional gradient phase methods<sup>20,38</sup> and brute-force numerical optimizations.<sup>39,43</sup>

In this work, we perform inverse designs of CPA metasurfaces by solving the surface impedance satisfying the boundary condition determined by two coherent incident waves from two arbitrary angles and the desired total scattered waves. The engineering of evanescent waves in the scattered fields<sup>23,39,42–47</sup> without altering the desired far-field outputs provides significant freedom in the CPA metasurface design, making another functionality of coherent control of reflection with a single direction possible. It is demonstrated that excitation of unidirectional evanescent waves propagating along the surface in the direction of the incident-wave wavevector can be used to achieve single-direction output in coherently controlled optical devices. Furthermore, a mathematical optimization method based on scattered harmonics analysis<sup>47</sup> is utilized to find the surface-impedance profile that simultaneously ensures the CPA and coherent maximum reflection (CMR) in a single direction. Thereafter, the substrate parameters are invoked as additional degrees of freedom in the optimization model, realizing reflection efficiency of 100%. As an example, we experimentally validate the CPA gradient metasurface design in microwaves by engineering the Indium Tin Oxide (ITO) film mounted on a grounded dielectric substrate. It is showed that the normalized output power can be continuously controlled between 0 and 1 by tuning the phase of the control wave.

## Results

### 2.1. Design Concept

Let us consider an impenetrable reciprocal lossy metasurface whose surface is periodically modulated along the  $x$ -direction, with the period  $D_x$ . The surface is in the  $xy$ -plane of a Cartesian coordinate system (see Figure 1). The metasurface is simultaneously illuminated by two transverse electric (TE)-polarized plane waves  $I_1$  and  $I_2$  at the incidence angles  $\theta_1$

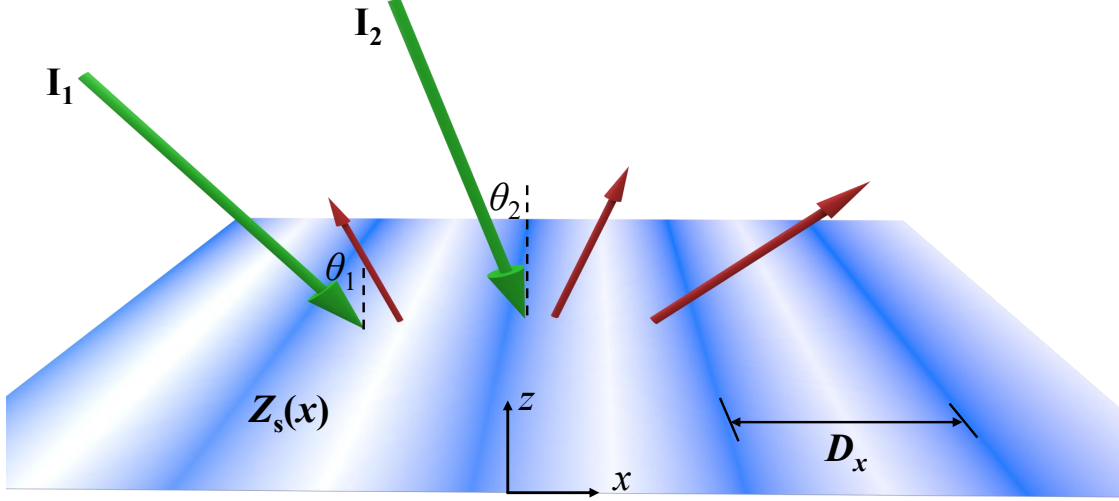


Figure 1: General scattering scenario for a periodically modulated impenetrable impedance surface. Two coherent beams  $I_1$  and  $I_2$  are simultaneously incident from two angles.

and  $\theta_2$  ( $\theta_1 > \theta_2$ ). The electric field amplitudes of the two beams  $I_1$  and  $I_2$  is  $E_1 = E_0$  and  $E_2 = \alpha E_0$ , respectively ( $\alpha$  is the amplitude ratio). The phase difference between them is  $\Delta\phi=0$ , defined at the origin point ( $x = 0, z = 0$ ). The electromagnetic properties of the metasurface can be characterized by the locally-defined surface impedance that stands for the ratio of the tangential electric and magnetic field amplitudes at the surface plane  $Z_s(x) = E_t(x)/H_t(x)$ .

The field reflected by a periodically modulated metasurface can be interpreted as a sum of Floquet harmonics. The tangential wavenumber of the  $n$ -th harmonic is related to the period and the incident wavenumber  $k_0$  as  $k_{rxn} = k_0 \sin \theta_i + 2\pi n_i/D_x$ , where  $i = 1, 2$ . The corresponding normal component of the reflected wavenumber equals  $k_{rzn} = \sqrt{k_0^2 - k_{rxn}^2}$ . If  $|k_{rxn}|$  is greater than the incident wavenumber, the wave is evanescent and it does not contribute to the far field. For the harmonic wave satisfying  $|k_{rxn}| < k_0$ ,  $k_{rzn}$  is real, and this wave is propagating. The evanescent harmonics will be dissipated by the lossy surface and the propagating harmonics will propagate into the far-zone at the angles  $\theta_{rn} = \arcsin(k_{rxn}/k_0)$ . In order to achieve coherent perfect absorption, it is necessary (but not sufficient) to ensure that all the diffracted propagating modes of two beams have the same set of angles  $\theta_{rn}$ , that allows mutual cancellation, defining the period  $D_x = \lambda_0/(\sin \theta_1 - \sin \theta_2)$  (Section S1,

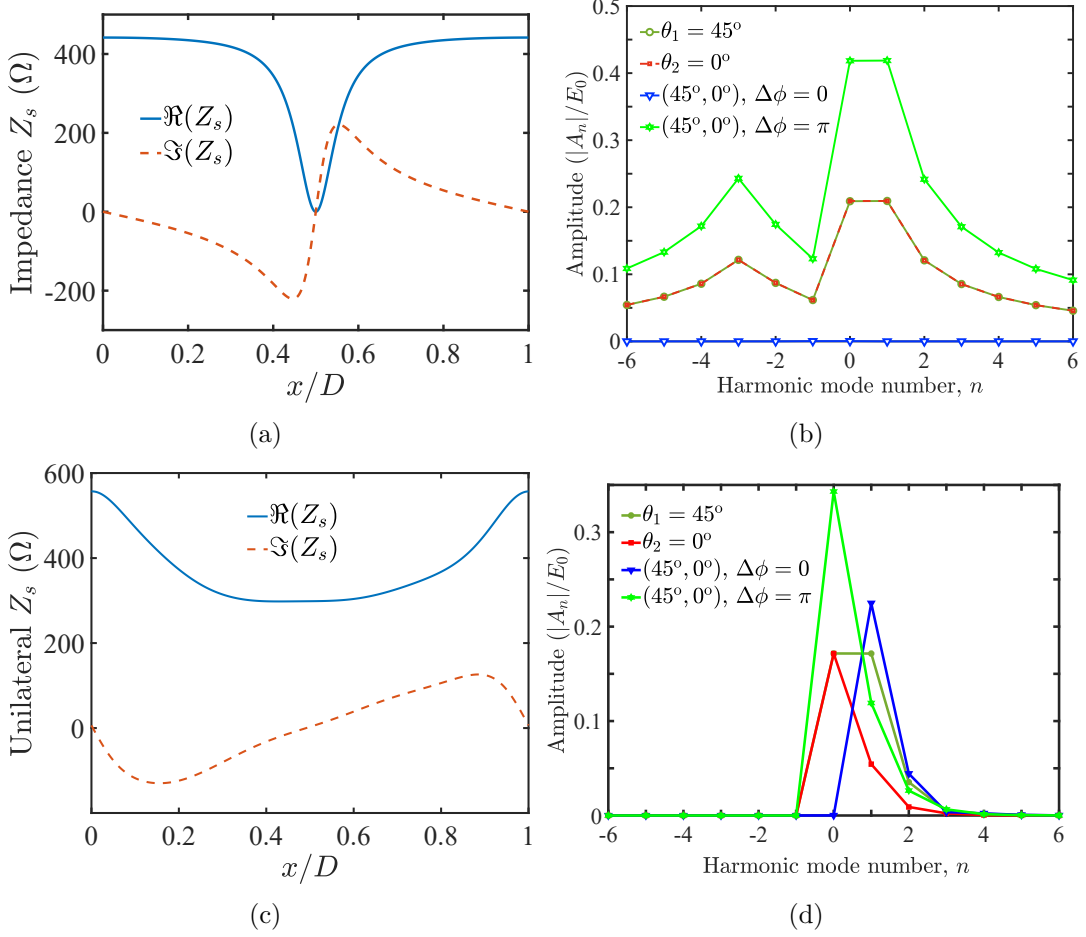


Figure 2: (a) Analytical surface impedance over one period to realize CPA for two incidence beams with  $(\theta_1, \theta_2) = (45^\circ, 0^\circ)$ . (b) Magnitudes of the complex amplitudes of different Floquet scattered harmonics (normalized by the amplitude of the incident electric field  $E_0$ ) when the gradient surface in (a) is illuminated by single-beam incidences at  $45^\circ$  and  $0^\circ$ , and for two-beam incidences in phase and out of phase, respectively. (c) Analytical unilateral surface impedance profile over one period to realize CPA for in-phase incidences and single-direction reflection for out-of-phase incidences. The Fourier coefficients of  $Y_s(x)$  read  $g_0 = 2.652 \times 10^{-3}$ ,  $g_1 = -7.769 \times 10^{-4}$ . (d) Amplitudes of scattered harmonics when the unilateral gradient surface in (c) is illuminated in those scenarios.

Supporting Information), where  $\lambda_0$  stands for the wavelength.

Our aim is to achieve coherent perfect absorption for two coherent in-phase waves simultaneously incident on the metasurface at two different angles  $\theta_1$  and  $\theta_2$ . First, let us assume that no evanescent waves are excited for these two illuminations. In the CPA case, there should be no reflected field at the surface. Thus, the tangential components of the total

electric field at the plane  $z = 0$  can be written as  $E_t(x) = E_0(e^{-jk_0 \sin \theta_1 x} + \alpha e^{-jk_0 \sin \theta_2 x})$ , where the time-harmonic dependency in the form  $e^{j\omega t}$  is assumed and suppressed. The corresponding total magnetic field reads  $H_t(x) = E_0(\cos \theta_1 e^{-jk_0 \sin \theta_1 x} + \alpha \cos \theta_2 e^{-jk_0 \sin \theta_2 x})/Z_0$ , with  $Z_0 = \sqrt{\mu_0/\epsilon_0}$  being the free-space wave impedance. The ratio of these electric and magnetic fields gives the required surface impedance

$$\begin{aligned} \Re(Z_s) &= Z_0 \frac{\cos \theta_1 + \alpha^2 \cos \theta_2 + \alpha \cos \Phi (\cos \theta_1 + \cos \theta_2)}{\cos^2 \theta_1 + \alpha^2 \cos^2 \theta_2 + 2\alpha \cos \theta_1 \cos \theta_2 \cos \Phi}, \\ \Im(Z_s) &= Z_0 \frac{\alpha (\cos \theta_1 - \cos \theta_2) \sin \Phi}{\cos^2 \theta_1 + \alpha^2 \cos^2 \theta_2 + 2\alpha \cos \theta_1 \cos \theta_2 \cos \Phi}, \end{aligned} \tag{1}$$

where  $\Phi = k_0(\sin \theta_1 - \sin \theta_2)x$  is the linearly varying phase. The real and imaginary parts of the surface impedance are even and odd functions of  $x$ , respectively. As is seen from Equations (1), the periodicity of the surface impedance is  $D = \lambda_0/(\sin \theta_1 - \sin \theta_2)$ , in accord with the above analysis. For passive metasurfaces, the real part of the surface impedance must be non-negative. Consequently, the amplitude ratio should satisfy  $\alpha \geq 1$  or  $\alpha \leq \cos \theta_1 / \cos \theta_2$  to ensure passive solution for CPA by the surface.

As an example, we consider two incident waves with incidence angles of  $(\theta_1, \theta_2) = (45^\circ, 0^\circ)$  and the same amplitude, assuming  $\alpha = 1$  for simplicity. (Other scenarios with  $(\theta_1, \theta_2) = (60^\circ, -30^\circ), (75^\circ, 15^\circ)$  are illustrated in Section S2 of Supporting Information, corresponding to different surface impedance profiles.) As is shown in Figure 2(a), everywhere on the surface its resistance is non-negative, demonstrating that passive gradient periodic surfaces can realize CPA for two asymmetric incident beams.

To analyze the mechanism of CPA by the periodic impedance surface further, we can determine the amplitudes of all the Floquet scattered harmonics for general plane-wave illumination, using the method reported in Ref.<sup>47</sup> The total reflected field can be represented

as an infinite sum of Floquet harmonic modes:

$$E_r = \sum_{n=-\infty}^{\infty} A_n e^{-jk_{rzn}z} e^{-jk_{rxn}x}, \quad (2)$$

where  $A_n$  is the complex amplitude of the  $n$ -th Floquet harmonic. Because the surface modulation is periodical, the surface admittance  $Y_s(x) = 1/Z_s(x)$  can be expanded into Fourier series:

$$Y_s(x) = \sum_{n=-\infty}^{+\infty} g_n e^{-j2n\pi x/D}. \quad (3)$$

A Toeplitz matrix  $\mathbf{Y}_s$  which we call the *admittance matrix* is determined only by the Fourier coefficients of the modulation function and filled with  $\mathbf{Y}_s(r, c) = g_{r-c}$  at the  $r$ -th row and  $c$ -th column (Section S4, Supporting Information). The reflection matrix is found as<sup>48</sup>

$$\mathbf{\Gamma} = (\mathbf{Y}_0 + \mathbf{Y}_s)^{-1} (\mathbf{Y}_0 - \mathbf{Y}_s), \quad (4)$$

where  $\mathbf{Y}_0 = \mathbf{Z}_0^{-1}$  is a diagonal matrix with its main entry representing the admittance of each space harmonic, which is  $\mathbf{Y}_0(n, n) = k_{rzn}/\omega_0\mu_0$ . The amplitudes  $A_n$  of reflected harmonics for a given  $m$ -th order Floquet harmonic of the incident wave can be calculated as  $A_n = \mathbf{\Gamma}(n, m)$ . Note that  $\mathbf{\Gamma}$  is a  $(2N+1) \times (2N+1)$  square matrix and the columns and rows of  $\mathbf{\Gamma}$  are indexed from  $-N$  to  $+N$ . The number  $2N+1$  of harmonics should be large enough to include all the propagating modes. A larger truncation limit can only improve the accuracy of calculation of higher-order evanescent modes, with little influence on the propagating modes that are of interest. When the surface is illuminated by two waves simultaneously, the amplitudes of all the Floquet harmonics are linear superpositions of all harmonics.

As is seen from Figure 2(b), when the two incident waves are in phase, all the harmonics have zero amplitude, meaning that CPA with no reflected fields occurs. However, when the two incident waves are out of phase, the reflected harmonics come out, including both propagating modes and evanescent ones, proving that the perfect absorption effect is phase-

coherent, different from perfect absorption for two angles.<sup>49</sup> To understand the mechanism of CPA in the metasurface better, the harmonics of the reflected field when single beams illuminate the surface separately are calculated. As shown in Figure 2(b), the complex amplitudes of every scattered harmonic are equal and  $180^\circ$  out of phase (the phases are shown in Section S3 of Supporting Information) for  $45^\circ$  and  $0^\circ$  incidences, resulting in destructive cancellation when the two beams illuminate simultaneously in phase. Here, the propagating harmonic of the order  $n = 0$  is defined at the specular direction of  $\theta_1$  for both incidences. Thus, the  $n = -1$  harmonic propagation direction is at the specular direction for  $0^\circ$  incidence. By properly designing the metasurface with the periodicity of  $D = \lambda_0/(\sin \theta_1 - \sin \theta_2)$ , three propagating modes corresponding to  $n = 0, -1, -2$  are created, and all the diffracted modes for both incidences have the same wavevectors, ensuing coherent interference for all corresponding harmonics. In the out-of-phase incidence case, the amplitudes of all the scattered harmonics double as compared to the single-beam case, as shown in Figure 2(b).

The analytical method to solve the surface impedance boundaries used above is based on the objective to realize CPA with the amplitudes of both scattered propagating and evanescent harmonics being zero when two coherent beams illuminate the metasurface simultaneously. Indeed, the amplitudes of evanescent surface modes can be nonzero without breaking the CPA condition, because they do not radiate into the far zone and their power will be dissipated at the lossy surface. Thus, the solution of the surface impedance to achieve CPA is not unique if a certain set of evanescent waves with unknown complex amplitudes is excited<sup>45</sup>. In addition to CPA, we invoke another functionality of coherent control of reflection with single direction, i.e. eliminating the unwanted outgoing beams at  $n = -1, -2$  orders and keeping the  $n = 0$  order with the maximal amplitude, when the two coherent incident beams are out-of-phase. In some applications, e.g. all-optical computing,<sup>1,2</sup> it is vital to achieve maximum reflected power, i.e., CMR, at the  $n = 0$  order and eliminate parasitic reflections which may cause undesired noise. In this case, finding the complex amplitudes of infinite numbers of evanescent modes for each incidence scenario is difficult or even im-

possible. Thus, instead of using the analytical method of calculating the surface impedance profile according to the total fields on the boundary, we find a surface impedance profile that simultaneously ensures the coherent control for absorption and reflection, inverting the scattering matrix calculation. First, the metasurface is modelled as in Equation (3). To suppress propagating modes at the negative orders ( $n = -1, -2$ ) and ensure that only the reflection channel at  $45^\circ$  is open, the Fourier series of the surface admittance  $Y_s(x)$  are set to be unilateral as  $Y_s(x) = \sum_{n=0}^{+\infty} g_n e^{-j2n\pi x/D}$  with only non-negative-order series coefficients being nonzero. This setting is reasonable because the unilateral surface admittance, making the admittance matrix  $\mathbf{Y}_s$  a lower triangular matrix, leads to the reflection matrix  $\mathbf{\Gamma}$  also being a lower triangular matrix. Note that the matrix  $\mathbf{\Gamma}$  is calculated by performing summation, inversion, and product operations between two lower triangular matrices  $\mathbf{Y}_0$  and  $\mathbf{Y}_s$ , as is seen from Equation (4), with the lower triangularity preserved.<sup>50</sup> Consequently, the scattered modes contain non-zero components of  $n \geq 0$  orders for  $45^\circ$  incidence and  $n \geq -1$  orders for  $0^\circ$  incidence, respectively. Then the specular reflection for normal incidence  $\Gamma_{-1,-1}$  is also zero because the amplitude should be equal to the scattered component at  $n = -1$  order for  $45^\circ$  incidence, which is zero under the CPA constraint. This effect highlights the role of unidirectional evanescent fields as a mechanism of suppressing propagating modes at the negative orders ( $n = -1, -2$ ). Owing to the unilateral impedance setting, the complicated matrix operations can be simplified due to the lower triangularity. The components of the reflection matrix for the lower propagating orders can be easily calculated as  $\Gamma_{-1,-1} = (y_0 - g_0)/(y_0 + g_0)$ , and  $\Gamma_{0,0} = (y_0 \cos 45^\circ - g_0)/(y_0 \cos 45^\circ + g_0)$ , where  $y_0 = 1/377 \text{ S}$  is the admittance of free space. When CPA is required, we have  $\Gamma_{0,-1} + \Gamma_{0,0} = 0$ . Since we have  $\Gamma_{-1,-1} = 0$ , the coefficient  $g_0$  is calculated as  $g_0 = y_0 = 2.652 \times 10^{-3}$ . Thus the reflections at  $n = 0$  order for  $45^\circ$  and  $0^\circ$  incidences are obtained as  $\Gamma_{0,0} = -0.1716$  and  $\Gamma_{0,-1} = 0.1716$ . The coefficient  $g_1$  can also be solved analytically as  $g_1 = y_0 \cos 45^\circ - g_0 = -7.769 \times 10^{-4}$  (See the detailed analysis in Section S4 of Supporting Information). Therefore, for impenetrable lossy metasurfaces with unidirectional evanescent modes, when CPA for two in-phase inci-

dences and single-direction reflection for two out-of-phase incidences are required, the two lower Fourier coefficients  $g_0$  and  $g_1$  are analytically determined. Moreover, the combined reflection amplitude at  $45^\circ$  for two anti-phase beams is always 0.3432. In this CPA metasurface via unidirectional evanescent modes excitation, the higher-order coefficients  $g_n (n \geq 2)$  only affect the evanescent modes, which can be arbitrary numbers while the passivity constraint  $\Re(Y_s) \geq 0$ , i.e.,  $\Re(g_0) \geq \sum_{n=1}^{+\infty} |g_n|$  is satisfied.

Figure 2(c) shows the typical solution of the surface impedance with only two non-zero coefficients  $g_0$  and  $g_1$ . The calculated amplitudes of scattered harmonics for single-beam incidences at  $45^\circ$  and  $0^\circ$ , and for two-beam incidences in phase and out of phase, for the impedance profile in Figure 2(c), are given in Figure 2(d), revealing the unilateral characteristic of scattering. The propagating components at  $n = -1, -2$  orders are suppressed successfully by exciting the unidirectional evanescent wave. The only remaining propagating reflected channel is  $n = 0$  order at the outgoing angle of  $45^\circ$ . When two incoming beams are in phase, the reflected propagating harmonic ( $n = 0$ ) of each beam cancel each other because they have the same amplitude and  $\pi$ -reflection-phase difference. Distinct from the zero-amplitude of all the harmonics for the in-phase CPA scenario in Figure 2(b), the CPA in Figure 2(d) occurs with non-zero-amplitude evanescent modes in the  $n \geq 1$  orders. The amplitude of reflected electric field at  $45^\circ$  ( $n = 0$ ) is doubled into 0.3432 when two incoming beams are out of phase ( $\Delta\phi = \pi$ ). We can conclude that the reflected power at  $45^\circ$  can be continuously controlled by phase tuning of the control beam. When the two beams are out of phase, the reflected power normalized by the incident beam power at  $45^\circ$  has the reflection efficiency of 11.78 %.

## 2.2. Practical design with a substrate

Low efficiency of the above design based on the impenetrable impedance model calls for optimization with the help of additional degrees of freedom. One possibility can be the use of one or more parameters of the actual implementation of the metasurface. In general,

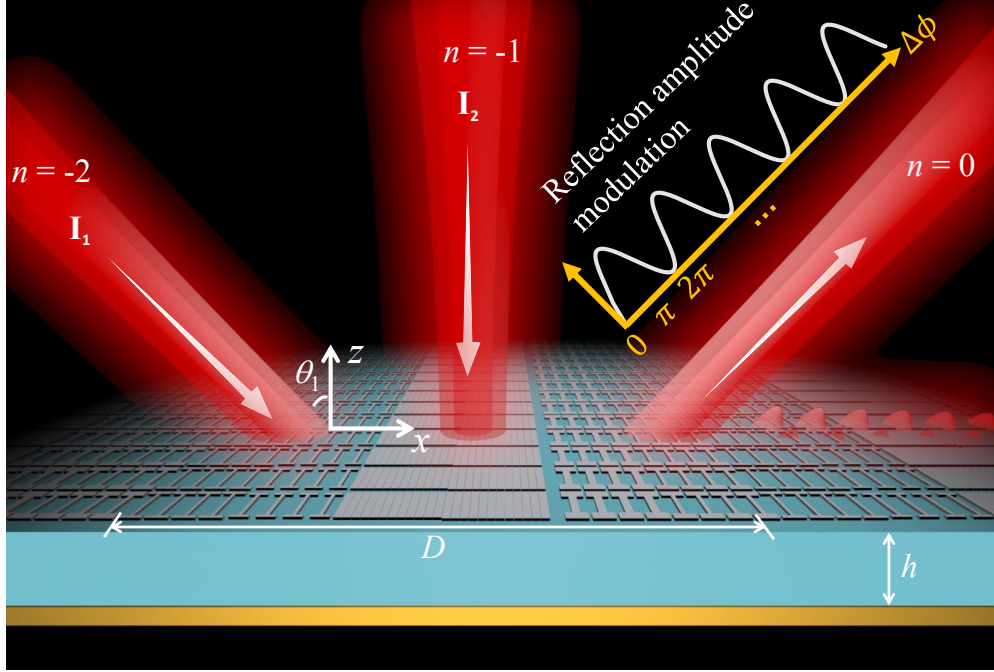


Figure 3: Schematics of reflection amplitude modulation for two coherent waves with the phase difference  $\Delta\phi$  incident on a periodic sheet over a grounded dielectric slab. The amplitude of the output beam is modulated continuously by varying  $\Delta\phi$ , and switched between 0 (coherent perfect absorption) and 1 (coherent maximum reflection) when  $\Delta\phi$  is switched between even and odd multiples of  $\pi$ .

the impedance surface in the impenetrable model used above can be realized as a periodic metal pattern on a thin grounded dielectric slab, as shown in Figure 3. The structure can be considered as a grid admittance of the top pattern with a shunt admittance of the grounded substrate. The characteristic admittance matrix  $\mathbf{Y}_d$  of the grounded substrate contains only diagonal terms  $\mathbf{Y}_d(n, n)$ , where  $\mathbf{Y}_d(n, n)$  is the admittance of the  $n$ -th harmonic, and it is expressed as

$$\mathbf{Y}_d(n, n) = k_{rzn}^d / [j\mu_0\omega_0 \tan(k_{rzn}^d h)], \quad (5)$$

where  $k_{rzn}^d = \sqrt{\omega_0^2 \epsilon_0 \epsilon_d \mu_0 - k_{rxn}^2}$  is the normal component of the wavevector in the substrate (see Equation S23 of the Supplemental Material of<sup>47</sup>),  $\epsilon_d$  and  $h$  are the permittivity and thickness of the substrate, respectively. The reflection matrix is calculated as  $\mathbf{\Gamma} = (\mathbf{Y}_0 + \mathbf{Y}_g + \mathbf{Y}_d)^{-1}(\mathbf{Y}_0 - \mathbf{Y}_g - \mathbf{Y}_d)$ , where  $\mathbf{Y}_g$  is the grid admittance matrix, which is a Toeplitz matrix determined by the Fourier coefficients (Section S5, Supporting Information).

The evanescent fields engineering is quite limited in the impenetrable model, resulting in a low reflection efficiency (11.78 %) in the out-of-phase scenario. In order to implement CPA with a high reflection efficiency, we need to use the substrate parameters as additional degrees of freedom in the design. Since the admittance of the grounded substrate with a moderate thickness strongly depends on the harmonic number, solving the grid impedance and substrate parameters becomes not straight-forward due to the complicated matrix operations. Thus, a mathematical optimization algorithm based on the scattering matrix calculation<sup>47</sup> is applied to search for an optimum solution for the grid impedance profile and substrate thickness.

The period of impedance sheet modulation is also set to  $D = \lambda_0 / \sin 45^\circ$ , with three propagating channels at  $-45^\circ$ ,  $0^\circ$ , and  $45^\circ$ . The Fourier series of the grid admittance is set to be unilateral as  $Y_g(x) = g_0 + g_1 e^{-j2\pi x/D}$ , ensuring that only the reflection channel at  $45^\circ$  is open for  $45^\circ$  incidence. In the optimization process, two Fourier terms  $g_0$  and  $g_1$  with four unknowns (the real and imaginary parts) are considered here to reduce complexity. The substrate thickness  $h$  is another unknown, and an available substrate with the permittivity  $\epsilon_d = 5.8(1 - j0.002)$  is used. The optimization goal is formulated as 6 objectives, including  $(|A_0|, |A_{-1}|, |A_{-2}|) = (0, 0, 0)$  for the in-phase scenario, and  $(|A_0|, |A_{-1}|, |A_{-2}|) = (A_{0\max}, 0, 0)$  for the out-of-phase scenario, where  $A_{0\max}$  is the maximum magnitude of reflection in the out-of-phase case. The constraints  $\Re(Y_g) \geq 0$ , i.e.,  $\Re(g_0) \geq |g_1|$  are imposed to ensure the grid to be a passive metasurface. Additionally, to make the reactance easier to implement by patterning a thin conductive surface, another constraint  $\Im(g_0) \geq |g_1|$  is set to ensure that the surface reactance is always capacitive at all points of the metasurface. (See more details in Section S10 in Supporting Information).

The maximum magnitude of reflection  $A_{0\max}$  in the out-of-phase scenario is about 1.022, and it is set as an optimization target. The value of  $A_{0\max} = 1.022$  is a fundamental limit of reflection amplitude at  $45^\circ$ , when CPA for two in-phase incident waves at the angles of  $(45^\circ, 0^\circ)$  and single-direction reflection for out-of-phase incidences are required for passive

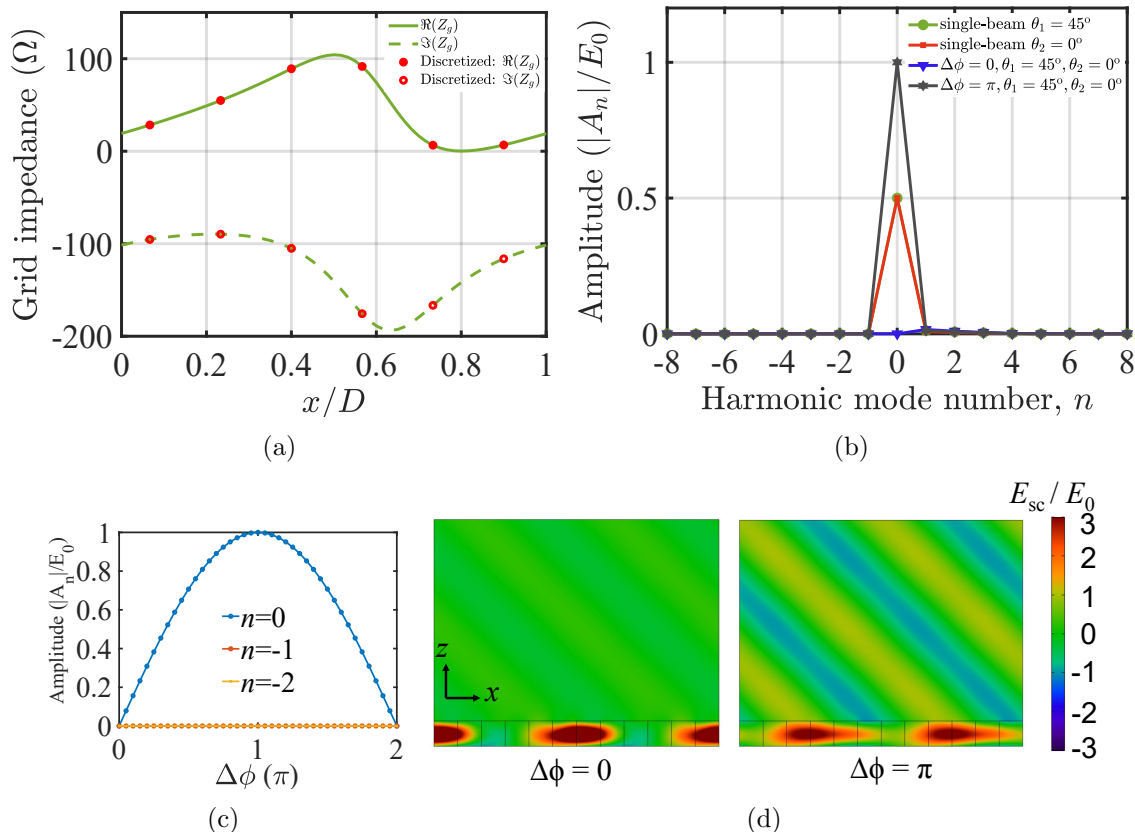


Figure 4: (a) The optimized and discretized grid impedance distribution over one period. (b) Amplitudes of the scattered harmonics when the optimized gradient metasurface is illuminated by a single beam at  $45^\circ$  and  $0^\circ$ , and for two-beam in-phase and out-of-phase illuminations, respectively. (c) The normalized amplitudes of three propagating harmonics ( $n = 0, -1, -2$ ) with a varying phase difference  $\Delta\phi$  between incidences at  $45^\circ$  and  $0^\circ$ . (d) The scattered electric fields for the metasurface modeled by the discretized grid impedance (step-wise approximation, 6 subcells per period) on top of a grounded dielectric substrate. Two plane-wave incidences are in phase (left) and out of phase (right).

metasurfaces (see detailed analysis in Section S5 of Supporting Information). Nearly a half of the total incoming power is still absorbed by the lossy surface in the coherent maximum reflection (CMR) scenario, since the essential interplay between the beams and the resistive surface causes inevitable absorption. Nonetheless, the substrate design provides an important additional degree of freedom to realize the desired optimum reflection properties, compared with the impenetrable surface. Similarly, in many metagratings with perfect anomalous reflections,<sup>32–34</sup> the metal-backed dielectric substrates are also invoked and optimized to achieve unitary coupling efficiencies. The optimized Fourier coefficients of the grid

admittance  $Y_g(x)$  read  $g_0 = (2.599 + 7.054j) \times 10^{-3}$  and  $g_1 = (-0.807 + 2.463j) \times 10^{-3}$ . The optimal substrate thickness is  $h = 0.2525\lambda_0$ . The required grid impedance which is passive and capacitive along the metasurface is shown in Figure 4(a).

Next, we analyse the scattered harmonics for the designed impedance sheet on the metal-backed dielectric substrate [see Figure 4(b)]. The reflection coefficient of the metasurface has the same magnitude of 0.5 at  $n = 0$  order for  $45^\circ$  and  $0^\circ$  single-beam incidences, resulting from destructive interference when these two beams are in phase. For the out-of-phase scenario, the normalized magnitude of the reflected field at  $n = 0$  order ( $45^\circ$ ) is about unity, which means that the reflected power efficiency reaches 100% (normalized by the incoming power of the  $45^\circ$  beam). Parasitic reflections into other directions ( $n = -1, -2$ ) are seen to be negligible. The evanescent harmonics are also unidirectional, but quite weak with the magnitude of 0.008 at  $n = 1$  order. In case of impenetrable surfaces, the role of the optimized evanescent harmonics is to redistribute power along the surface, ensuring local passivity. In case if there is a substrate and the sheet is penetrable, the role can be played by optimized waveguide fields inside the substrate. For this reason, the same result (CPA) can be achieved with rather small evanescent fields over the surface. Figure 4(c) illustrates the phase-controlled modulation of reflections at three propagating orders. The reflection coefficient at  $45^\circ$  can be continuously controlled from 0 to 1 by phase tuning, with the other two parasitic reflections maintained very close to zero. See the Supplemental Animation<sup>51</sup> for the switch of reflected beam by an incident phase-controlled wave.

In implementations, the influence of discretization on the metasurface performance is an important factor (see detailed analysis of scattered harmonics versus the number of subcells in Section S6 of Supporting Information). We use six subcells over a period and each discretized impedance value is set at the central point of each subcell, as shown in Figure 4(a). The scattered fields from the ideal impedance sheet on the metal-backed dielectric slab for both in-phase and out-of-phase incidences are presented in Figure 4(d), using full-wave simulations in Comsol. The reflected field distribution confirms that the metasurface with six subcells

per period possesses the desired response: nearly perfect absorption with reflected power fraction of only 0.05% for two in-phase illuminations and nearly total reflection at  $45^\circ$  for two out-of-phase illuminations, relative to the intensity of the  $45^\circ$  incidence. It is seen that the top lossy sheet and reflective ground separated by the slab act as a leaky-wave cavity with enhanced fields. For the in-phase scenario, the direct reflections of the top surface and leaky wave components of the cavity destructively cancel out, and all the power is absorbed by the lossy surface, causing CPA. By changing the initial phase difference between the two coherent incidences into  $\pi$ , constructive interference occurs among these components, resulting in maximum reflection.

### 2.3. Physical implementation and experimental validation

The theory above is general and applies to any frequency from microwaves to visible bands.<sup>52</sup> We choose a microwave realization as a proof of concept. The required impedance profile at 15.22 GHz is realized using an ITO film with the surface resistance of  $5.5 \Omega/\text{sq}$  supported by a grounded dielectric slab with the thickness  $h = 4.95 \text{ mm}$ , as shown in Figure 3. The detailed parameters and structures of each unit cell are presented in the Supporting Information(Section S8). Due to the resolution limitation of picosecond laser micro-processing, the complex grid impedance is implemented as six subcells, and each subcell is divided into four equal sub-subcells in order to make the local design of the gradient impedance more robust. By structuring the homogeneous resistive ITO film into I-shaped cells, the required grid resistance and reactance on a surface in Figure 4(a) can be created. For  $y$ -polarization incident waves, such I-shaped resonators can be modeled as RLC series circuits. The required resistance is realized by tailoring the width and length of the ITO strips. Smaller width and longer length result in higher grid resistance. The required reactance can be tailored by adjusting capacitance of the gap, which can be increased by narrowing the gap or increasing the length or width of the bar, with a small influence on the resistive part. The 5th and 6th subcells degenerate into strips, to implement resistive parts as close to the theoretical

value as possible. However, there are still deviations of  $3.6 \Omega$  and  $1.1 \Omega$  from the theoretical resistances of the 5th and 6th subcells, respectively. The deviation can be eliminated if an ITO film with a lower surface resistance is utilized. To simplify the fabrication process, we neglect this deviation. The impact is analyzed theoretically, showing that the reflected power fraction in the in-phase scenario increases from 0.05% to 0.4%, which is tolerable in most practical situations. Since the two beams with  $0^\circ$  and  $45^\circ$  incidence angles illuminate the surface simultaneously, all the elements should have angle-independent surface impedances. The I-shaped resonators have angle-insensitive impedance under TE incidences, satisfying this requirement.<sup>53</sup> In the strips of the 5th and 6th subcells, narrow slits are cut out to reduce the angular sensitivity of the impedance.

Figure 5(a) shows the simulated frequency response of the metasurface for the normal and  $45^\circ$  incidences. For the normal illumination, strong reflections occur at  $n = -1$  and  $n = 0$  harmonics (denoted as  $\xi_{-1}$  and  $\xi_0$ ), and the amplitude of the  $n = -2$  scattered propagating mode is nearly zero in the whole frequency band. The reflection at the  $n = -1$  mode (specular reflection at  $0^\circ$ ) also has a near-zero dip at the design frequency of 15.22 GHz, and the reflection efficiency at the  $n = 0$  mode (anomalous reflection at  $0^\circ$ ) is about 13.9% (the relative amplitude is 0.44). Note that for anomalous reflection, the efficiency is calculated as  $\xi = (E_r/E_i)^2 \cos \theta_r / \cos \theta_i$ .<sup>39</sup> For the  $45^\circ$  illumination, the reflections at both  $n = -1$  and  $n = -2$  modes ( $\xi'_{-1}$  and  $\xi'_{-2}$ ) are close to zero, and the efficiency at the  $n = 0$  mode ( $\xi'_0$ ) is about 21% at 15.22 GHz (the relative amplitude is 0.46). Therefore, at the operating frequency 15.22 GHz, the reflected modes for both incidences at the outgoing angle of  $45^\circ$  are almost equal-amplitude, satisfying the condition of CPA. When the two illumination beams are in phase, the total scattered fields are quite small (the relative amplitude of 0.02), indicating nearly perfect coherent absorption. However, when the two illuminations are switched into the out-of-phase state, the relative amplitude of the scattered fields is about 0.91, and the coherent maximum reflection is mainly along the  $45^\circ$  direction, in good agreement with the simulated results of the ideal model in Figure 4(d). (See Section S9 of

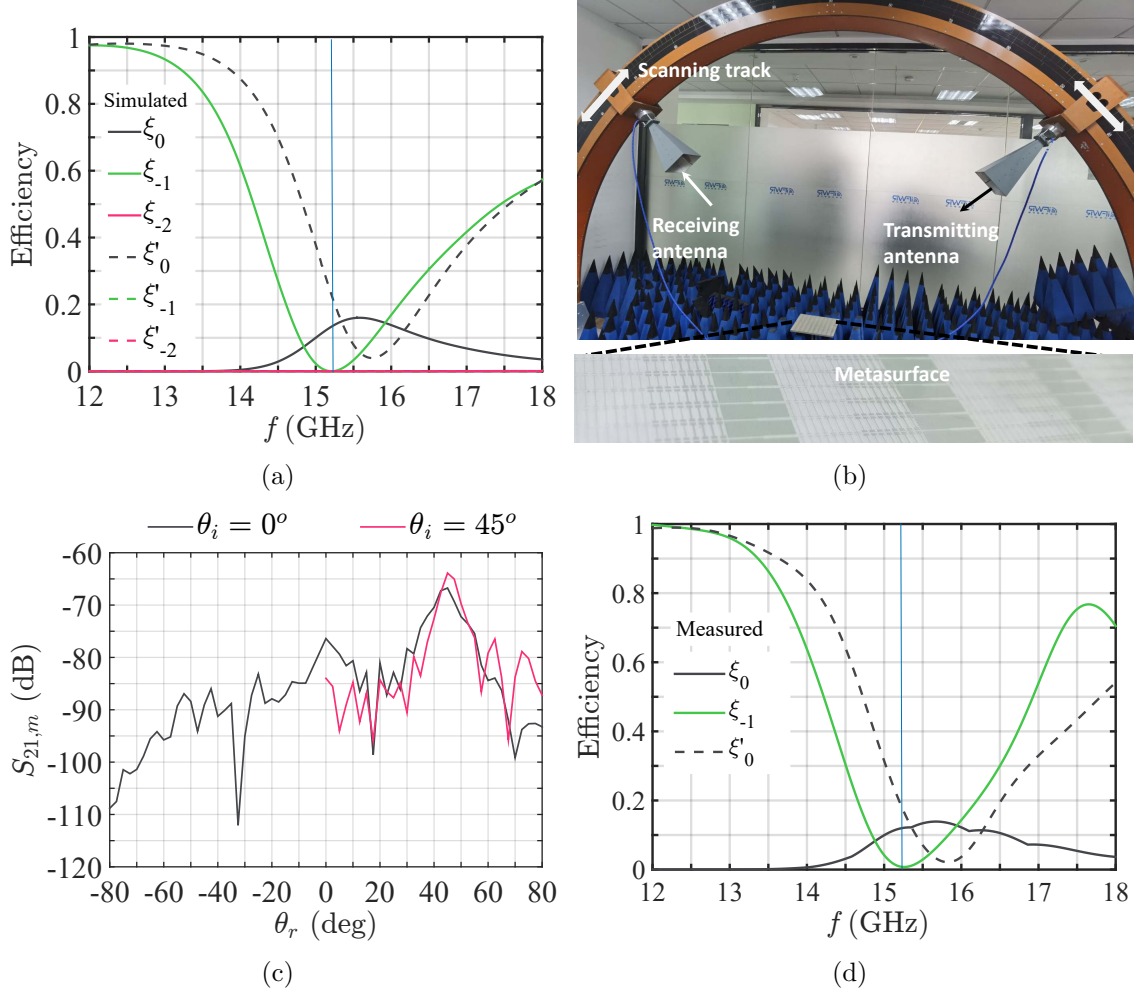


Figure 5: (a) Simulated and (d) measured reflection efficiency spectrum for different diffracted modes of each single beam at  $0^\circ$  (solid lines) and  $45^\circ$  (dashed lines). (b) Schematic of the experimental setup (top) and photograph of the fabricated sample (bottom). (c) Signals at 15.22 GHz measured by the receiving antenna at different orientation angles with the transmitting antenna at  $0^\circ$  and  $45^\circ$ .

Supporting Information for more detailed figures.)

We have fabricated a sample (see Methods) and carried out several experiments to validate the theoretical results (see Figure 5(b)). First, the transmitting antenna is fixed at  $0^\circ$ , whereas the receiving antenna is moved along the scanning track with a step of  $2.5^\circ$ . The signal reflected from the metasurface is measured by the receiving antenna at different angles  $\theta_r$ . Then, the transmitting antenna is fixed at  $45^\circ$  and the receiving antenna is scanning its position to measure the reflected signal in the other half space. The reflected signals at the

negative reflection angles for  $45^\circ$  incidence cannot be measured because the two antennas cannot be moved into the same half space, but according to the simulations these signals should be at a very low level. As shown in Figure 5(c), the main peaks of reflections for both two incidences occur at  $\theta_r = 45^\circ$ , which is an expected result according to the theory and simulations. There is another reflection peak at  $\theta_r = 0^\circ$  for the normal incidence case at 15.22 GHz, which is about  $-10$  dB lower than the main peak. The specular reflection power is about 10% of the power at  $45^\circ$ .

To estimate the amplitude efficiency of the metasurface at all three reflection channels, we replaced the metasurface by a copper plate of the identical size and measured the specular reflection signal amplitudes from the reference uniform metal mirror for  $\theta_i = 2.5^\circ$  (approximately normal incidence),  $22.5^\circ$ , and  $45^\circ$  incidence angles. The specular reflection efficiency of the metasurface for  $0^\circ$  and  $45^\circ$  illuminations are calculated by normalizing the signal amplitude by the amplitude of the signal reflected from the reference plate, illuminated at  $2.5^\circ$  and  $45^\circ$  angles, respectively. As shown in Figure 5(d), at the design frequency of 15.22 GHz, the specular reflection efficiencies at  $0^\circ$  and  $45^\circ$  ( $\xi_{-1}$  and  $\xi'_0$ ) equal 0.8% and 18.6% (the relative amplitude is 0.431), respectively. For the normal incidence, the anomalous reflection angle at the  $n = 0$  mode is dependent on the frequency as  $\theta_r = \arcsin(15.22/(\sqrt{2}f))$ , which equals  $45^\circ$  at 15.22 GHz and varies from  $63.7^\circ$  to  $36.7^\circ$  as the frequency changes from 12 GHz to 18 GHz. Therefore, to obtain the reflection efficiencies at anomalous directions for different frequencies, we adopt the received signals at different angles  $\theta_r$ . The reflected signal amplitudes from the reference uniform metal mirror at different incidence angle  $\theta_r/2$  are used for normalization, since the angle between the transmitting and receiving antennas is identical with the anomalous deflection angle  $\theta_r$  of the metasurface. Additionally, we divide the obtained amplitude by an estimated correction factor<sup>39</sup>  $\sqrt{\cos(\theta_r)}/\cos(\theta_r/2)$ , which gives the ratio between the theoretically calculated signal amplitudes from an ideal metasurface (of the same size and made of lossless materials) and a perfectly conducting plate. At the design frequency of 15.22 GHz, the correction factor is equal to 0.91, thus

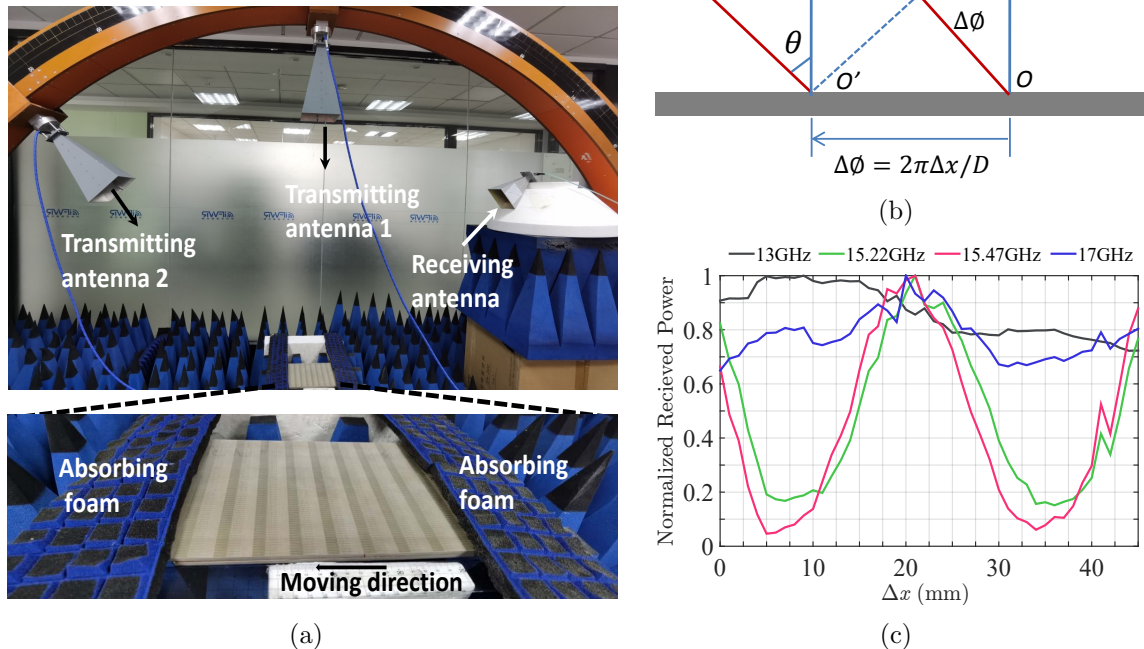


Figure 6: (a) Experimental setup. Two transmitting antennas fed via a power divider illuminate the metasurface normally and at  $45^\circ$ . A receiving antenna is placed at  $45^\circ$  to measure the total reflected power. Two pieces of absorbing foam are put on both sides, ensuring that the effective exposure area of the metasurface remains fixed when the surface is shifted. (b) The reference point  $O$  is the intersection point of the  $0^\circ$  and  $45^\circ$  beams on the metasurface when the phase difference is 0. The phase difference at a distance  $\Delta x$  from the reference point  $O$  is  $\Delta\phi = 2\pi\Delta x/D$ , which is linearly varying as a function of the horizontal distance  $\Delta x$ . (c) The normalized received power for different metasurface positions at 13, 15.22, 15.47, and 17 GHz.

the reflection efficiency is calculated as 12% (the relative amplitude is 0.412), as shown in Figure 5(d). The measured efficiency is in good agreement with the results obtained using numerical simulations (see Figure 5(a)), except for some ripples in the  $\xi_0$  curve caused by the discrete angular scanning step in the measurement. The relative amplitudes of reflections for both incidences at the  $n = 0$  mode are almost equal in the measurements, verifying the capability for CPA.

To experimentally verify the phase-controlled reflection by the metasurface, in the last measurement shown in Figure 6(a), two transmitting antennas fed via a power divider illuminate the metasurface normally and at  $45^\circ$ . A receiving antenna is placed at the  $45^\circ$  angle to

measure the total power reflected by the metasurface under two simultaneous illuminations. To avoid severe insertion loss caused by the use of a phase shifter in one branch, which may increase the amplitude inequality between two beams, we mimic the phase-difference-tuning process by moving the metasurface along the  $x$  direction. With respect to a certain fixed point along the metasurface period (e.g.,  $x = 0$ ), only the phase of the obliquely incident beam is affected by this lateral translation, and the phase of the normally incident beam remains unchanged. Therefore, as seen in Figure 6(b), the phase difference between the two beams defined at a fixed reference point is linearly varying when the metasurface is translated laterally. To ensure the effectively-illuminated area of the metasurface to remain stable during the moving process, we put two pieces of absorbing foam on top of both sides of the sample. The total received power, normalized by the maximum power of reflected wave is changing with varying the distance  $\Delta x$ . As is seen in Figure 6(c), the modulation depths reach 0.15 and 0.04 at 15.22 GHz and 15.47 GHz, respectively. This result indicates that coherent enhancement and cancellation near the design frequency can be achieved by tuning the phase difference of the two incident beams. The period of the modulation is about 29 mm, almost equal to the period of the metasurface, which validates the theoretical analysis. However, at the frequency far from the designed one, for instance at 13 GHz and 17 GHz, the coherent phenomenon becomes much weaker, as is seen in Figure 6(c), due to a mismatch of the main reflection angles and the reflection amplitudes of the normally and obliquely incident waves.

## Conclusions

We have demonstrated coherent perfect absorption of two beams incident at arbitrary angles. It has been found that this effect is possible for relative beam amplitudes within a certain range using a gradient passive planar structures. When these two incident beams change into the out-of-phase state, reflections at all three propagating channels come out.

To realize coherent control of reflection with a single direction, the other reflections can be suppressed by engineering excitation of unidirectional evanescent modes. To realize a larger reflection for the out-of-phase scenario, we use an optimization algorithm to search for an optimum solution for the grid impedance profile and the substrate thickness, which is powerful when many degrees of freedom are used in a multi-channel metasurface design. In other design methodologies such as non-local metasurfaces<sup>39</sup> and plasmonic gratings,<sup>28,54</sup> where the interference between all the elements of a unit cell are important for the device performance, a brute-force optimization process in full-wave simulations is required, which is time consuming and even cannot work when multiple input beams and multi-functionalities for multiple channels are required. Compared with them, our approach is much more robust and efficient for realizing coherent control of multiple beams (even more than two beams), since the metasurface is inversely designed by solving for the surface impedance satisfying the boundary condition determined by arbitrary coherent incident waves from arbitrary angles and the desired scattered waves. By introducing unidirectional evanescent modes in the scattered field, parasitic reflections are eliminated or minimized. Moreover, the angular dependence of the surface impedance of the substrate is also considered in the proposed algorithm, which is vital in metasurface design for multiple-angle incidence scenarios.<sup>55,56</sup>

We have realized a gradient metasurface with angular-asymmetric coherent perfect absorption and reflection functionalities. The concept of wave control via evanescent harmonics engineering and independent control of the electromagnetic response for multiple illuminations can be applied for engineering multi-functional wave processes. Metasurface-based designs are attractive in practical applications. For example, by placing a planar structure on a metal-grounded dielectric layer, the velocity or position of the object can be detected by monitoring the total reflection of such a object under two coherent illuminations. Additionally, we hope that this work can find promising applications in phased-array antennas, one-side detection and sensing, and optical switches with low insertion loss.

## Additional notes on the experiment

**Design and modeling of the metasurface:** The prototype was designed for operation at 15.22 GHz. The impedance sheet is discretized into 6 sub-cells, and each sub-cell is divided into 4 identical sub-sub-cells. The effective grid impedance of each sub-sub-cell is retrieved from the simulated reflection coefficient ( $S_{11}$ ) using the locally periodic approximation and the transmission-line method approach (see Section S7 of Supporting Information). Numerical simulations are carried out using a frequency-domain solver, implemented by CST Microwave Studio. Excitations propagating along the  $z$ -direction from port 1 with the electric field along the  $y$ -direction and the magnetic field along the  $x$ -direction are used in the simulations to obtain the  $S_{11}$  parameter. The dimensions of all the elements in the unit cells are designed and optimized one by one to fit the theoretically found required surface impedance.

Once the dimensions of all the elements in the unit cells are found, we perform numerical simulations of the unit cell for the normal and  $45^\circ$  incidences. The simulation domain of the complete unit cell was  $D \times D_y \times D$  (along the  $x, y,$  and  $z$  directions), the unit cell boundary condition and the Floquet ports were set. The scattered fields for the normal and  $45^\circ$  incidences were calculated by subtracting the incident waves from the total fields. Finally, the total scattered fields when the metasurface is illuminated by two waves simultaneously were obtained by adding the scattered field of each single beam with different phase differences.

**Realization and measurement:** The ITO pattern of the metasurface was manufactured using the picosecond laser micromachining technology (ST600UV from Nanjing Site Laser) on a 0.175-mm-thick ITO/PET film. The sample comprises 10 unit cells along the  $x$  axis and 66 unit cells along the  $y$  axis [Figure 5(b)] and has the size of  $14.15\lambda \times 10.04\lambda = 278.9 \text{ mm} \times 198 \text{ mm}$ . The ITO/PET film was adhered to a 4.95-mm-thick F4BTM substrate with  $\epsilon = 5.8(1 - j0.01)$  backed by a copper ground plane.

The operation of the designed metasurface was tested using a NRL-arc setup [Figure 5(b)]. In the experiment, two double-ridged horn antennas with 17 dBi gain at 15.22 GHz are

connected to a vector network analyzer as the transmitter and receiver. The metasurface was located at a distance of 2 m (about  $101\lambda$ ) from both the transmitting and receiving antennas where the radiation from the antenna can be approximated as a plane wave. The antennas are moved along the scanning track to measure the reflection towards different angles. Time gating is employed to filter out all the multiple scattering noise signals received by the antenna.

## **Supporting Information**

Supporting Information is available from the Wiley Online Library or from the author.

## **Acknowledgements**

The authors are grateful to Dr. Viktor S. Asadchy for useful discussions. S.M.Z. acknowledges support from China Scholarship Council. This research was also supported by the Natural Science Foundation of Zhejiang Province(LY22F010001), Natural Science Foundation of Ningbo (2022J098), and the Fundamental Research Funds for the Provincial Universities of Zhejiang.

## **Conflict of Interest**

The authors declare no conflict of interest.

## **Data Availability Statement**

The data that support the findings of this study are available in the Supporting Information of this article.

## Keywords

gradient metasurface, coherent perfect absorption, coherent control, evanescent wave, inverse design

## References

- (1) Fu, Y.; Hu, X.; Lu, C.; Yue, S.; Yang, H.; Gong, Q. All-optical logic gates based on nanoscale plasmonic slot waveguides. *Nano Lett.* **2012**, *12*, 5784–5790.
- (2) Fang, X.; Tseng, M. L.; Ou, J. Y.; Macdonald, K. F.; Tsai, D. P.; Zheludev, N. I. Ultrafast all-optical switching via coherent modulation of metamaterial absorption. *Appl. Phys. Lett.* **2014**, *104*, 141102.
- (3) Shi, J.; Fang, X.; Rogers, E. T. F.; Plum, E.; MacDonald, K. F.; Zheludev, N. I. Coherent control of Snell’s law at metasurfaces. *Opt. Express* **2014**, *22*, 21051–21060.
- (4) Papaioannou, M.; Plum, E.; Valente, J.; Rogers, E. T.; Zheludev, N. I. Two-dimensional control of light with light on metasurfaces. *Light Sci. Appl.* **2016**, *5*, e16070.
- (5) Papaioannou, M.; Plum, E.; Valente, J.; Rogers, E. T.; Zheludev, N. I. All-optical multichannel logic based on coherent perfect absorption in a plasmonic metamaterial. *APL Photonics* **2016**, *1*, 090801.
- (6) Fang, X.; MacDonald, K. F.; Zheludev, N. I. Controlling light with light using coherent metadevices: all-optical transistor, summator and inverter. *Light Sci. Appl.* **2015**, *4*, e292–e292.
- (7) Silva, A.; Monticone, F.; Castaldi, G.; Galdi, V.; Alù, A.; Engheta, N. Performing mathematical operations with metamaterials. *Science* **2014**, *343*, 160–163.
- (8) Achouri, K.; Lavigne, G.; Salem, M. A.; Caloz, C. Metasurface spatial processor for electromagnetic remote control. *IEEE Trans. Antennas Propag.* **2016**, *64*, 1759–1767.

- (9) Zhu, Z.; Yuan, J.; Jiang, L. Multifunctional and multichannel all-optical logic gates based on the in-plane coherent control of localized surface plasmons. *Opt. Lett.* **2020**, *45*, 6362–6365.
- (10) Kang, M.; Zhang, Z.; Wu, T.; Zhang, X.; Xu, Q.; Krasnok, A.; Han, J.; Alù, A. Coherent full polarization control based on bound states in the continuum. *Nat. Commun.* **2022**, *13*, 1–9.
- (11) Peng, P.; Mi, Y.; Lytova, M.; Britton, M.; Ding, X.; Naumov, A. Y.; Corkum, P.; Villeneuve, D. Coherent control of ultrafast extreme ultraviolet transient absorption. *Nat. Photonics* **2022**, *16*, 45–51.
- (12) Chong, Y. D.; Ge, L.; Cao, H.; Stone, A. D. Coherent perfect absorbers: time-reversed lasers. *Phys. Rev. Lett.* **2010**, *105*, 053901.
- (13) Wan, W.; Chong, Y.; Li Ge, H. N.; Stone, A. D.; Cao, H. Time-reversed lasing and interferometric control of absorption. *Science* **2011**, *331*, 889–892.
- (14) Dutta-Gupta, S.; Deshmukh, R.; Gopal, A. V.; Martin, O. J. F.; Gupta, S. D. Coherent perfect absorption mediated anomalous reflection and refraction. *Opt. Lett.* **2012**, *37*, 4452–4454.
- (15) Baranov, D. G.; Krasnok, A.; Shegai, T.; Alù, A.; Chong, Y. Coherent perfect absorbers: linear control of light with light. *Nat. Rev. Mater.* **2017**, *2*, 17064.
- (16) Kita, S.; Takata, K.; Ono, M.; Nozaki, K.; Kuramochi, E.; Takeda, K.; Notomi, M. Coherent control of high efficiency metasurface beam deflectors with a back partial reflector. *APL Photonics* **2017**, *2*, 046104.
- (17) Xomalis, A.; Demirtzioglou, I.; Plum, E.; Jung, Y.; Nalla, V.; Lacava, C.; MacDonald, K. F.; Petropoulos, P.; Richardson, D. J.; Zheludev, N. I. Fibre-optic metadvice

- for all-optical signal modulation based on coherent absorption. *Nat. Commun.* **2018**, *9*, 182.
- (18) Wang, C.; Sweeney, W. R.; Stone, A. D.; Yang, L. Coherent perfect absorption at an exceptional point. *Science* **2021**, *373*, 1261–1265.
- (19) Li, S.; Luo, J.; Anwar, S.; Li, S.; Lu, W.; Hang, Z. H.; Lai, Y.; Hou, B.; Shen, M.; Wang, C. Broadband perfect absorption of ultrathin conductive films with coherent illumination: superabsorption of microwave radiation. *Phys. Rev. B* **2015**, *91*, 220301(R).
- (20) Yu, N.; Genevet, P.; Kats, M. A.; Aieta, F.; Tetienne, J.-P.; Capasso, F.; Gaburro, Z. Light propagation with phase discontinuities: generalized laws of reflection and refraction. *science* **2011**, *334*, 333–337.
- (21) Sun, S.; He, Q.; Xiao, S.; Xu, Q.; Li, X.; Zhou, L. Gradient-index meta-surfaces as a bridge linking propagating waves and surface waves. *Nat. Mater.* **2012**, *11*, 426–431.
- (22) Kildishev, A. V.; Boltasseva, A.; Shalaev, V. M. Planar photonics with metasurfaces. *Science* **2013**, *339*, 1232009.
- (23) Epstein, A.; Eleftheriades, G. V. Synthesis of passive lossless metasurfaces using auxiliary fields for reflectionless beam splitting and perfect reflection. *Phys. Rev. Lett.* **2016**, *117*, 256103.
- (24) Cao, Y.; Fu, Y.; Zhou, Q.; Ou, X.; Gao, L.; Chen, H.; Xu, Y. Mechanism behind angularly asymmetric diffraction in phase-gradient metasurfaces. *Physical Review Applied* **2019**, *12*, 024006.
- (25) Tan, Q.; Zheng, B.; Cai, T.; Qian, C.; Zhu, R.; Li, X.; Chen, H. Broadband spin-locked metasurface retroreflector. *Adv. Sci.* **2022**, *9*, 2201397.
- (26) Hao, H.; Ran, X.; Tang, Y.; Zheng, S.; Ruan, W. A single-layer focusing metasurface based on induced magnetism. *Prog. Electromagn. Res* **2021**, *172*, 77–88.

- (27) Fan, Z.; Qian, C.; Jia, Y.; Wang, Z.; Ding, Y.; Wang, D.; Tian, L.; Li, E.; Cai, T.; Zheng, B.; Kaminer, I.; Chen, H. Homeostatic neuro-metasurfaces for dynamic wireless channel management. *Sci. Adv.* **2022**, *8*, eabn7905.
- (28) Yoon, J. W.; Koh, G. M.; Song, S. H.; Magnusson, R. Measurement and modeling of a complete optical absorption and scattering by coherent surface plasmon-polariton excitation using a silver thin-film grating. *Phys. Rev. Lett.* **2012**, *109*, 257402.
- (29) Jung, M. J.; Han, C.; Yoon, J. W.; Song, S. H. Temperature and gain tuning of plasmonic coherent perfect absorbers. *Opt. Express* **2015**, *23*, 19837–19845.
- (30) Yoon, J. W.; Jung, M. J.; Song, S. H. Gain-assisted critical coupling for high-performance coherent perfect absorbers. *Opt. Lett.* **2015**, *40*, 2309–2312.
- (31) Ra’di, Y.; Sounas, D. L.; Alù, A. Metagratings: beyond the limits of graded metasurfaces for wave front control. *Phys. Rev. Lett.* **2017**, *119*, 067404.
- (32) Epstein, A.; Rabinovich, O. Unveiling the properties of metagratings via a detailed analytical model for synthesis and analysis. *Phys. Rev. Appl.* **2017**, *8*, 054037.
- (33) Popov, V.; Boust, F.; Burokur, S. N. Controlling diffraction patterns with metagratings. *Phys. Rev. Appl.* **2018**, *10*, 011002(R).
- (34) Wong, A. M. H.; Eleftheriades, G. V. Perfect anomalous reflection with a bipartite Huygens’ metasurface. *Phys. Rev. X* **2018**, *8*, 011036.
- (35) Fu, Y.; Shen, C.; Cao, Y.; Gao, L.; Chen, H.; Chan, C. T.; Cummer, S. A.; Xu, Y. Reversal of transmission and reflection based on acoustic metagratings with integer parity design. *Nature Commun.* **2019**, *10*, 1–8.
- (36) Zhang, Z.; Kang, M.; Zhang, X.; Feng, X.; Xu, Y.; Chen, X.; Zhang, H.; Xu, Q.; Tian, Z.; Zhang, W., et al. Coherent perfect diffraction in metagratings. *Adv. Mater.* **2020**, *32*, 2002341.

- (37) Xu, G.; Eleftheriades, G. V.; Hum, S. V. Analysis and design of general printed circuit board metagratings with an equivalent circuit model approach. *IEEE Trans. Antennas Propag.* **2021**, *69*, 4657–4669.
- (38) Sun, S.; Yang, K.-Y.; Wang, C.-M.; Juan, T.-K.; Chen, W. T.; Liao, C. Y.; He, Q.; Xiao, S.; Kung, W.-T.; Guo, G.-Y., et al. High-efficiency broadband anomalous reflection by gradient meta-surfaces. *Nano Lett.* **2012**, *12*, 6223–6229.
- (39) Díaz-Rubio, A.; Asadchy, V. S.; Elsakka, A.; Tretyakov, S. A. From the generalized reflection law to the realization of perfect anomalous reflectors. *Sci. Adv.* **2017**, *3*, e1602714.
- (40) He, T.; Liu, T.; Xiao, S.; Wei, Z.; Wang, Z.; Zhou, L.; Cheng, X. Perfect anomalous reflectors at optical frequencies. *Sci. Adv.* **2022**, *8*, eabk3381.
- (41) Cuesta, F. S.; Ptitsyn, G. A.; Mirmoosa, M. S.; Tretyakov, S. A. Coherent retroreflective metasurfaces. *Phys. Rev. Res.* **2021**, *3*, L032025.
- (42) Cuesta, F. S.; Kuznetsov, A. D.; Ptitsyn, G. A.; Wang, X.; Tretyakov, S. A. Coherent asymmetric absorbers. *Phys. Rev. Appl.* **2022**, *17*, 024066.
- (43) Wang, X.; Díaz-Rubio, A.; Asadchy, V. S.; Ptitsyn, G.; Generalov, A. A.; Alalaurinaho, J.; Tretyakov, S. A. Extreme asymmetry in metasurfaces via evanescent fields engineering: angular-asymmetric absorption. *Phys. Rev. Lett.* **2018**, *121*, 256802.
- (44) Kwon, D.-H.; Tretyakov, S. A. Perfect reflection control for impenetrable surfaces using surface waves of orthogonal polarization. *Phys. Rev. B* **2017**, *96*, 085438.
- (45) Kwon, D.-H. Lossless scalar metasurfaces for anomalous reflection based on efficient surface field optimization. *IEEE Antennas Wireless Propag. Lett.* **2018**, *17*, 1149–1152.
- (46) Kwon, D.-H. Lossless tensor surface electromagnetic cloaking for large objects in free space. *Phys. Rev. B* **2018**, *98*, 125137.

- (47) Wang, X.; Díaz-Rubio, A.; Tretyakov, S. A. Independent control of multiple channels in metasurface devices. *Phys. Rev. Appl.* **2020**, *14*, 024089.
- (48) Hwang, R.-B. *Periodic structures: mode-matching approach and applications in electromagnetic engineering*; John Wiley & Sons, 2012.
- (49) Zhirihin, D.; Simovski, C.; Belov, P.; Glybovski, S. Mushroom high-impedance metasurfaces for perfect absorption at two angles of incidence. *IEEE Antennas Wireless Propag. Lett.* **2017**, *16*, 2626–2629.
- (50) Drazin, M. P.; Dungey, J. W.; Gruenberg, K. W. Some theorems on commutative matrices. *Journal of the London Mathematical Society* **1951**, *s1-26*, 221–228.
- (51) See Supplemental Animation.
- (52) Asadchy, V. S.; Wickberg, A.; Díaz-Rubio, A.; Wegener, M. Eliminating scattering loss in anomalously reflecting optical metasurfaces. *ACS Photon.* **2017**, *4*, 1264–1270.
- (53) Luukkonen, O.; Simovski, C.; Granet, G.; Goussetis, G.; Lioubtchenko, D.; Raisanen, A. V.; Tretyakov, S. A. Simple and accurate analytical model of planar grids and high-impedance surfaces comprising metal strips or patches. *IEEE Trans. Antennas Propag.* **2008**, *56*, 1624–1632.
- (54) Chen, X.; Li, M.; Chen, W.; Yang, H.; Pei, Z.; Li, E.-P.; Chen, H.; Wang, Z. Broadband janus scattering from tilted dipolar metagratings. *Laser Photonics Rev.* **2022**, *16*, 2100369.
- (55) Zhang, X.; Li, Q.; Liu, F.; Qiu, M.; Sun, S.; He, Q.; Zhou, L. Controlling angular dispersions in optical metasurfaces. *Light Sci. Appl.* **2020**, *9*, 1–12.
- (56) Yuan, Y.; Cheng, J.; Fan, F.; Wang, X.; Chang, S. Control of angular dispersion in dielectric gratings for multifunctional wavefront shaping and dynamic polarization conversion. *Photon. Res.* **2021**, *9*, 2190–2195.